16th World Congress in Computational Mechanics (WCCM)
21-26 July 2024, Vancouver, Canada
A. Korobenko, M. Laforet, S. Prudhomme, R. Vaziri (Eds)

DISCRETIZATION ERROR ESTIMATION FOR FLOW SIMULATIONS USING GENERAL HYBRID GRIDS

YANNIS KALLINDERIS[1]

[1] Laboratory of Aerodynamic Design of Air Vehicles,
Department of Mechanical and Aeronautical Engineering,
University of Patras, 26504 Rio, Greece ,
kallind@alum.mit.edu

Key words: flow field simulations, discretization error, hybrid grids, grid quality, flow sensors, adaptive grids

Abstract. A primary area of the author's work with his students is outlined in the present article. It regards the estimation of the discretization error with mixed-element and adaptive meshes. Use of general hybrid meshes for computational flow simulations is of importance due to the complexity of both the geometry and the fields. The meshes can consist of a mix of hexahedra, prisms and tetrahedra with pyramids being transitional elements. The discretization error is a primary component of the numerical error in flow simulations. Primary factors affecting it are the local density of the mesh, as well as its "distortions", namely the variation in local size and orientation (stretching, skewness), the shape of the individual elements (shear, twist), and the local change in their type (grid interfaces). Two distinct approaches have been followed in order to estimate and control the discretization error. The grid-based ("a priori") approach assesses mesh quality from the analytic expression of the truncation error. The solution-based ("a posteriori") approach monitors approximations of the variation of flow quantities ("sensors"). Those are then applied to guide adaptation of the grid to the simulated flow field.

1 INTRODUCTION

Use of general hybrid meshes for computational flow simulations [1] is of importance due to the complexity of both the geometry and the fields. The meshes can consist of a mix of hexahedra, prisms and tetrahedra with pyramids being transitional elements. Those types of elements are arranged in areas of different grid density and directionality according to the local flow and geometry features.

General hybrid meshes necessitate fast and robust techniques for their generation [2-4], element-type independent solvers for incompressible [5-7] and compressible flows [8, 9], as well as parallel flow simulations [10] with emphasis on partitioning / load balancing for those heterogenous meshes [11, 12]. Further, general methods for grid adaptation are required. All major techniques for automatically adapting the mesh to the flow field and geometry have been pursued [13-15]. Those include local divisions / coarsening, redistribution as well as automatic regeneration of the entire mesh. Adapting the mesh to the geometry curvature included use of

local curved-edge quadratic elements [16].

The discretization error is a major component of the numerical error in flow simulations. Primary factors affecting it are the local density of the mesh, as well as its "distortions", namely the variation in local size and orientation (stretching, skewness), the shape of the individual elements (shear, twist), and the local change in their type (grid interfaces) [17, 18].

Two distinct approaches have been followed in order to estimate and control the discretization error: the grid-based ("a priori") methods are employed during grid generation (e.g. [19, 20]), while the solution-based ("a posteriori") ones monitor the simulated flow field and guide mesh improvement (adaptation) (e.g. [21, 22]).

The grid-based approach utilizes a second order finite volume discretization of spatial derivatives. It derives expressions of the truncation error for the most commonly encountered "distortions" of the mesh and works with the terms that multiply the solution derivatives (grid metrics or error coefficients). The magnitude of those terms is used to guide grid generation and post-processing of the initially created grid.

The solution-based error estimation monitors approximations of the variation of a spectrum of flow quantities ("sensors"). Those are then applied to guide adaptation of the grid to the simulated flow field.

The present article is an outline of the author's work with his students on estimation of the discretization error with general hybrid and adaptive meshes.

2 GRID-BASED ERROR ESTIMATION

It is clear that generation of mixed-type meshes, as well as the use of diverse techniques for local adaptation necessitates groundwork on numerical error estimation. A mesh quality index is presented that is derived from the analytic expression of the truncation error related to first order spatial derivatives. The index was introduced in [19] for two-dimensional meshes and was generalized for three-dimensional hybrid grids in [20].

Figure **1** depicts the control volume of an example local hybrid mesh surrounding the vertex O. The truncation error (TE) in the calculation of the first order derivative of the scalar flow variable u at the vertex O is defined as:

$$\mathrm{TE}_i = u_{x_i}\Big|_{num} - u_{x_i} \quad , \quad i = x,y,z \tag{1}$$

where $u_{x_i}\Big|_{num}$ and u_{x_i} are the numerical and analytical values of the derivatives, respectively. The subscript i denotes the direction of the derivative.

The numerical value of the derivative is calculated with a vertex-centered finite volume discretization. A low order discretization is chosen so as to "bring out" the gross error. Substituting the numerical expression of the derivative, Equation (1) becomes:

$$\mathrm{TE}_i = \frac{1}{V}\sum_f \left(u\ S_i\right)_f - u_{x_i} \quad , \quad i = x,y,z \tag{2}$$

where the summation is over the cell faces (f) of the local control volume (V) surrounding the grid point of interest and S_x, S_y, S_z are the projected face-areas on the yz-, xz-, and xy-planes, respectively.

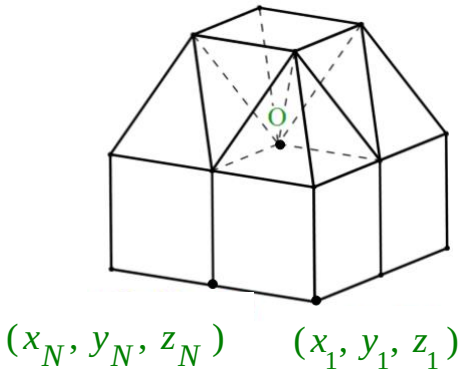

Figure 1: The control volume of a local mesh consisting of hexahedra, tetrahedra, and pyramids employed for the calculation of flow gradients at vertex O.

Using Taylor series expansion for the field variable u , the truncation error is cast in the following general form:

$$\mathrm{TE}_i = \left(e_{xx}\, u_{xx} + e_{yy}\, u_{yy} + e_{zz}\, u_{zz} + e_{xy}\, u_{xy} + e_{zx}\, u_{zx} + e_{zy}\, u_{zy} \right) + \ldots \ , \ i = x,y,z \qquad (3)$$

The first order error terms (e) contain grid metrics only and will be termed "error coefficients" in the following. Their general form corresponding to the derivative approximation in the i - direction is:

$$e_{x^p y^q z^r} = \frac{1}{V} \ \frac{k}{(p+q+r)!} \cdot \sum_f \left[\frac{1}{N} \cdot \left(\Delta X_1^{\,p} \Delta Y_1^{\,q} \Delta Z_1^{\,r} + \ldots + \Delta X_N^{\,p} \Delta Y_N^{\,q} \Delta Z_N^{\,r} \right) \cdot S_i \right]_f \qquad (4)$$

where N is the number of vertices which participate in the calculation. Also, p, q and r are integers equal to the order of the derivative of u with respect to x, y, and z, respectively. Finally, k is an integer coefficient from the Taylor expansion.

The error coefficients can then be employed to yield the value of a "mesh quality index" (Q). This is carried out using the absolute values of the *first order* error coefficients:

$$Q_i = \left| e_{xx} \right| + \left| e_{yy} \right| + \left| e_{zz} \right| + \left| e_{xy} \right| + \left| e_{zx} \right| + \left| e_{zy} \right| \quad , \ i = x,y,z \qquad (5)$$

where i denotes the calculation of the x, y, or z-spatial derivative of the field function. The above expression is normalized with a local characteristic length. It should be emphasized that higher values of the index Q indicate worse quality. The best value is zero, which denotes second order of accuracy.

3 ERROR AND MESH QUALITY

A general hybrid mesh for complex geometries and flow fields typically contains elements with stretching, skewness, shear, torsion (Figure 2), as well as interfaces between the different types of elements. These mesh "distortions" are primary contributors to the discretization error.

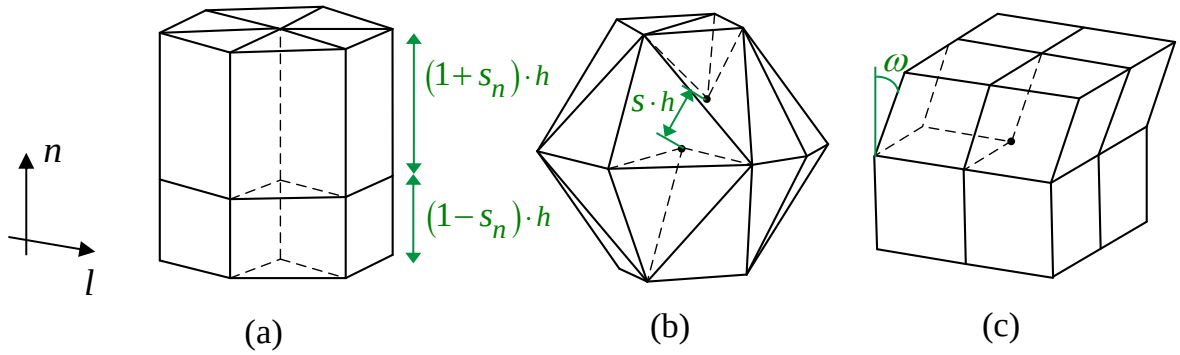

Figure 2: Examples of mesh distortions: (a) *normal* stretching of prism stacks, (b) *point* stretching of tetrahedral mesh, (c) skewness of hexahedral stacks.

Each mesh distortion type was directly related to the mesh quality index (Q) in [19, 20]. The "normal-to-the-wall" and the "lateral" directions are of relevance for boundary layer grids. Indicative examples are presented in this section. For hexahedral and prismatic meshes that exhibit stretching (s), the corresponding quality indices are:

$$Q_n = Q_l = \frac{1}{2}|s_n| + 2|s_l| \tag{6}$$

where s_n is the "normal-to-the-wall" stretching parameter and s_l is the "lateral" stretching parameter.

For the skewness case, the mesh quality indices for both the hexahedral and prismatic meshes are:

$$Q_n = Q_l = \frac{1}{2}\left|\cos(\omega)-1\right| + \frac{1}{2}\left|\frac{sin(2\omega)}{cos(\omega)+1}\right| \tag{7}$$

where ω is the skewness angle, defined in Figure 2 (c).

3.1 Hybrid grid interfaces

Change in the type of the elements creates special interfaces which require examination in terms of the local accuracy. The interfaces are encountered in regions of the grid with constant or variable number of hexahedral / prismatic layers. Figure 3 shows indicative examples of grid interfaces studied in [20], which correspond to boundary layer grids with constant number of

layers. The first two have element type change in the "normal" direction, while the third is an example of a "lateral" interface.

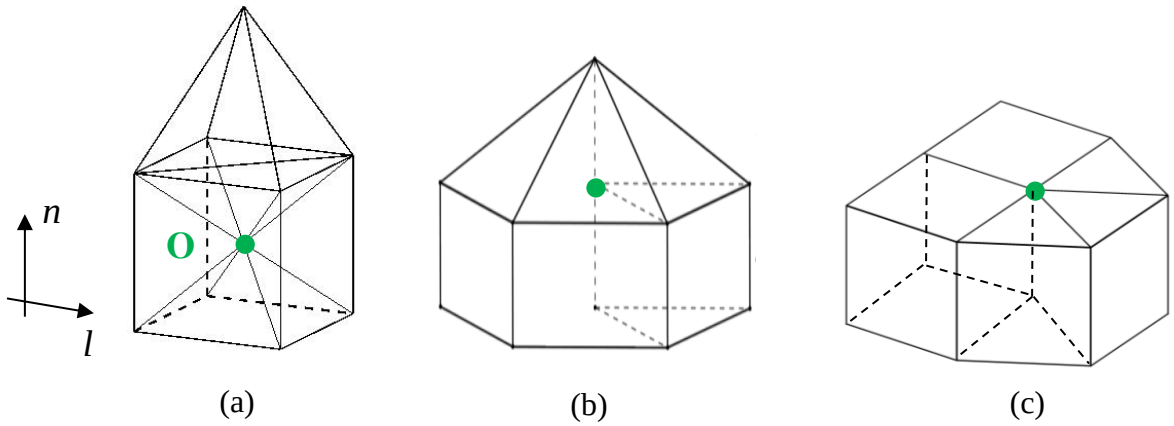

Figure 3: Grid interface configurations corresponding to boundary layer grid stacks with constant number of layers: (a) hexahedra and (b) prisms for "normal" type of interfaces, (c) mixed hexahedra and prisms ("lateral" interface type).

Use of variable number of layers is a common practice when the geometry includes gaps, local cavities or singular points. Figure 4(a) shows an example of an interface studied in [18], which corresponds to boundary layer grids with variable number of hexahedral layers. That example interface has element type change in both the "normal" and the "lateral" direction. The mesh quality, as quantified by the index Q_n, can be significantly improved with vertical displacement of the central point (O), as shown in Figure 4(b).

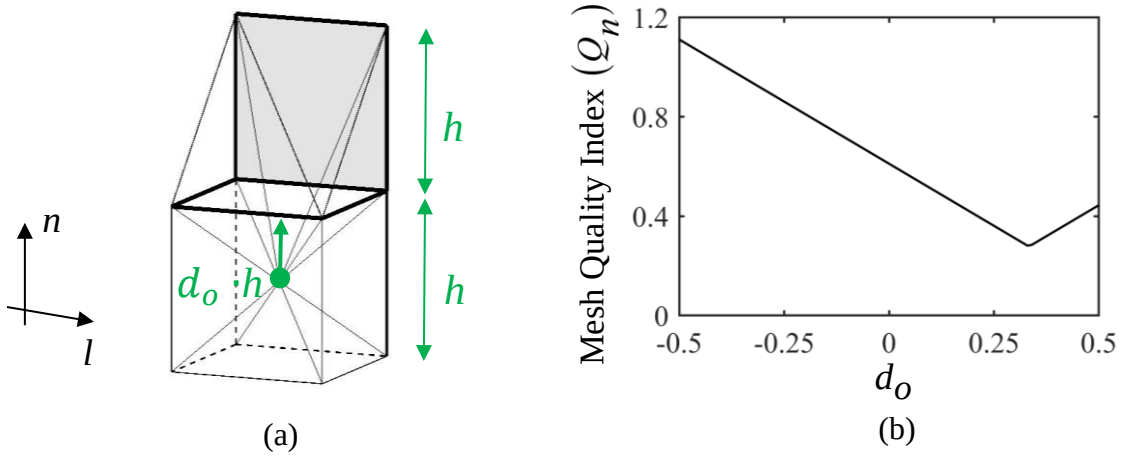

Figure 4: Vertical central point displacement (a) and corresponding quality improvement (reduction in Q_n) (b). Case of an interface with variable number of hexahedral layers.

Table 1 presents the values of the mesh quality index Q_n for the common hybrid grid interfaces of Figure 3 (top three rows of the table). It is observed that calculation of the "normal" derivative $(\partial u/\partial n)$ is less sensitive to the lateral variation of the type of elements. The second

part of the table shows appreciably higher values of Q_n for interfaces of meshes with variable number of layers.

Table 1: Mesh quality index in the "normal" direction (Q_n) for different interface types.

Interface types		Q_n
Constant number of layers	Hexahedra ("normal")	0.25
	Prisms ("normal")	0.25
	Mixed hexahedra and prisms ("lateral")	0.15
Variable number of layers	Hexahedra	0.61
	Prisms	0.28

4 SOLUTION-BASED ERROR APPROXIMATION: FLOW SENSORS

The analytic truncation error expression indicates larger discretization error where the flow field derivatives are high. Those derivatives are approximated by flow sensors. The target of the sensors is to detect multiple features of different strength in the same flow field. A general framework for development and evaluation of flow sensors was introduced in [21] and [22].

Evaluation of the sensors is based on their application to "prototype" flow fields. The sensor effectiveness (P_{eff}) is based on the degree of match between the region of the flow features and the region of the flow field flagged by the sensor.

Figure 5 depicts a typical sensor effectiveness diagram. The "cut off" value of the sensor above which the local flow region is flagged as containing significant gradients ("detection threshold") is a key factor for accurate detection. The primary characteristics of the effectiveness curve are its peak value $(P_{eff,\,max})$, its area (A_{eff}) and its sensitivity to the threshold value (T), i.e. maintenance of high P_{eff} with varying T.

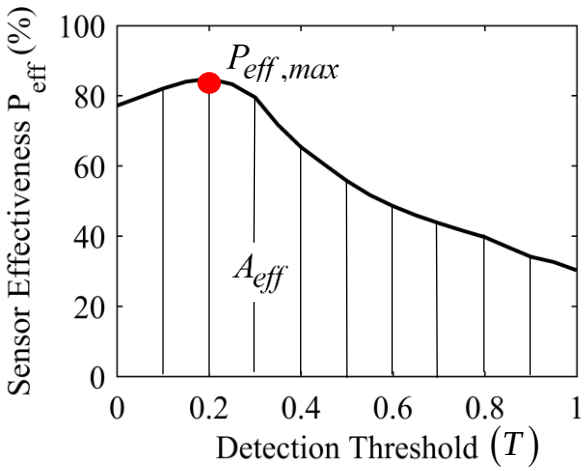

Figure 5: Typical flow sensor performance with varying threshold for flow feature detection.

4.1 General formulation of the sensors

The flow sensors are cast into a simple mathematical form that expresses spatial variation of a flow quantity (q). Specifically, the sensor (δq) is defined as the difference in the flow quantity q between the endpoints (i and j) of a grid edge:

$$\delta q = \left| \, q_i - q_j \, \right| \tag{8}$$

The algebraic combination of two single-quantity sensors $(\delta q,\ \delta r)$ leads to a new class of flow sensors, termed *composite* sensors $\left(C_{\delta q,\, \delta r}\right)$. They are introduced for the detection of multiple and interacting flow features of different strength. The *composite* sensors formula can be derived from a second order polynomial:

$$C_{\delta q,\, \delta r} = a_1 (\delta q)^2 + a_2 (\delta r)^2 + a_3 (\delta q)(\delta r) + a_4\, \delta q + a_5\, \delta r + a_6 \tag{9}$$

where the constants (a_i) are derived based on the desired characteristics of the sensor, by applying appropriate conditions. Two significant conditions, among others, are the following:

(i) $C_{\delta q,\, 0} = \delta q$, $C_{0,\, \delta r} = \delta r$.

Namely, if a feature is properly detected by one of the component sensors, it will also be detected by the *composite* sensor.

(ii) The *composite* sensor "switches off" for very strong features. This is quantified as:

$C_{1,1} = 0$.

This condition is included so that emphasis is given on weaker features of the flow field.

The final equation for the *composite* sensor, after application of the conditions, is:

$$C_{\delta q,\, \delta r} = \delta q \cdot (1 - \delta r) + \delta r \cdot (1 - \delta q) \tag{10}$$

Figure 6 represents the above equation.

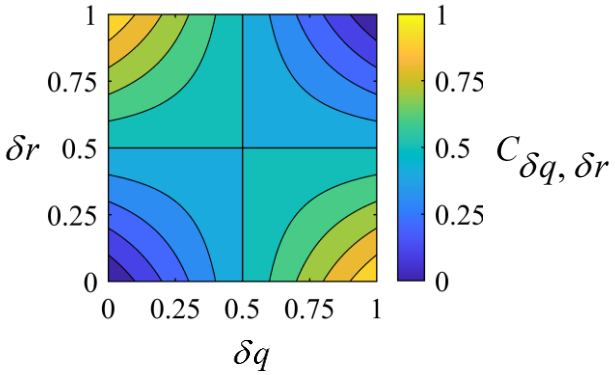

Figure 6: Distribution of composite sensor values $\left(C_{\delta q,\, \delta r}\right)$ with respect to its component sensors $(\delta q,\ \delta r)$.

4.2 Example applications to flow fields with multiple features

The example cases of this section are drawn from reference [22]. The first case is a supersonic flow in a duct with a high ramp angle (δ) of 22°, with the upper wall being assigned a "slip flow" condition. A Mach reflection configuration, a boundary layer and a slip line are the features encountered. Figure 7 shows the contours of two indicative single-quantity sensors, the vorticity (ω) and the pressure difference (δP), as well as the contour of the *composite* sensor $C_{\omega,\ \delta P}$. The *composite* sensor is the only one which captures all the features of the flow field.

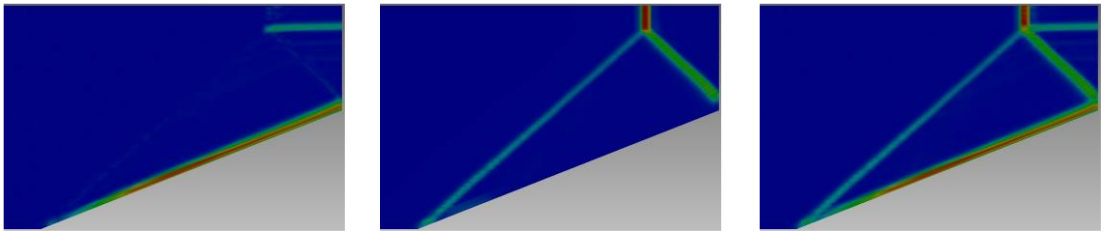

(a) (b) (c)

Figure 7: Contours of sensor fields: (a) vorticity (ω), (b) pressure difference (δP), (c) *composite* $\left(C_{\omega,\ \delta P}\right)$. The *composite* sensor captures all the flow features. Case of supersonic flow in a duct with a high ramp angle.

Figure 8 is an illustrative example of the improvement in the effectiveness, when using *composite* sensors. The effectiveness curves of the total velocity sensor (δU), as well as the curves of two indicative *composite* sensors based on δU are shown. The *composite* sensors exhibit a peak close to that of the single-quantity sensor δU, but with significantly less sensitivity to the threshold value variation.

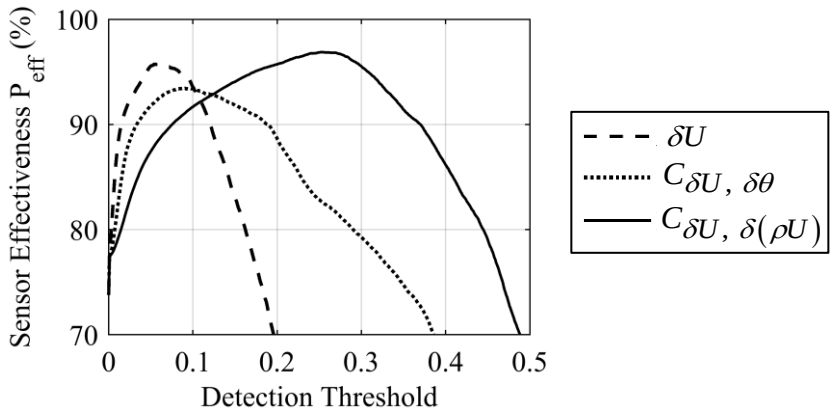

Figure 8: Employment of *composite* sensors improves the flow feature detection capability of traditional single-quantity ones. Case of supersonic flow in a duct with a high ramp angle $\left(M_\infty = 2.65,\ Re = 1.5\times10^4,\ \delta = 22^\circ\right)$.

The next sensors application example involves supersonic flow past a cylinder in a "slip-wall" duct. Contours of the total velocity field (U) are shown in Figure 9. A bow shock is observed, which reflects on the duct walls forming Mach stems and slip lines. A boundary layer and a wake behind the cylinder are also formed.

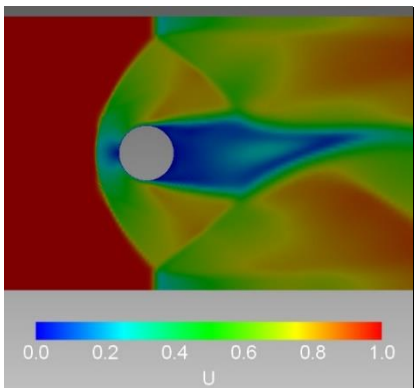

Figure 9: Velocity magnitude contours for the case of supersonic flow past a cylinder in a duct $(M_\infty = 2.8, Re_D = 500)$. The flow field exhibits a bow shock, Mach reflection configurations as well as a boundary layer and a wake.

Table 2 lists the performance of several sensors. The flow parameters involved are the total velocity (U), the entropy (s), the flow change of direction $(\delta\theta)$, as well as the change in temperature (δT). It is observed that both the peak effectiveness $(P_{eff,max})$ and the area under the effectiveness curve (A_{eff}) are higher for the *composite* indicators compared to the single-quantity sensor (δU).

Table 2: Performance metrics of the most effective sensors employed. Case of supersonic flow past a cylinder in a duct $(M_\infty = 2.8, Re_D = 500)$.

Sensor	$P_{eff,max}$ (%)	A_{eff}
δU	83.6	0.6
$C_{\delta s,\, \delta(\ln U)}$	89.4	1.2
$C_{\delta U,\, \delta\theta}$	87.4	1.7
$C_{\delta s,\, \delta\theta}$	87.4	1.0
$C_{\delta U,\, \delta(\ln U)}$	87.1	1.6
$C_{\delta(\ln U),\, \delta T}$	85.5	1.1

4.3 Flow statistics and automatic detection threshold

A primary issue with application of flow feature detection has been the automatic calculation of a threshold value for the sensor. A typical setting of its formula follows early work in [13]:

$$T_{auto} = \bar{s} + a \cdot \sigma \tag{11}$$

where $\bar{s}$ is the mean of the sensor values, σ is their standard deviation and a is a coefficient which is usually set empirically.

The correlations observed between the different statistical parameters of the sensors motivated their employment for the construction of an automatic detection threshold formula. Figure 10 depicts correlations between the statistical parameters of mean value $(\bar{s})$, standard deviation (σ), skewness squared $\left(\gamma_1{}^2\right)$ and kurtosis (β_2) of the sensor distributions. A pattern of linear correlation is observed between the statistical parameters.

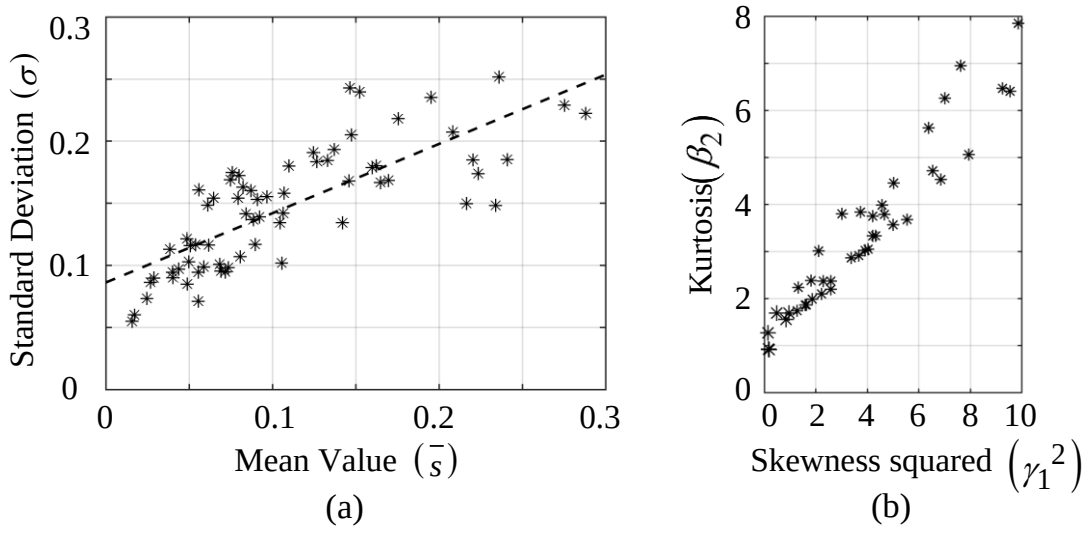

Figure 10: Correlation study between the sensor distribution parameters of mean value $(\bar{s})$, standard deviation (σ), skewness squared $\left(\gamma_1{}^2\right)$ and kurtosis (β_2) of the sensors. A pattern of linear correlation is observed in both graphs.

The above correlations led to the proposition of the following formula for the threshold parameter a [22]:

$$a = \begin{cases} 1 - 0.7\dfrac{\beta_2}{\gamma_1{}^2}\ , \gamma_1 > 1 \\ -1.1 \qquad\quad , \gamma_1 < 1 \end{cases} \tag{12}$$

5 CURRENT RELATED WORK

A priori improvement of a general hybrid grid is a current primary effort. It is based on the error coefficients and relies on local motions of the vertices of the various elements. The emphasis has been on the interfaces between the different types of elements within areas of viscous flow. Further, optimum combination of the different grid adaptation techniques including adaptive local use of quadratic elements is investigated.

Finally, a novel error sensitivity analysis is being carried out. Theoretical and numerical analysis is employed in order to assess the influence of primary factors of a simulation on the error. Those factors include the flow field parameters, the numerical solution itself, the boundary conditions, as well as characteristics of the geometry.

REFERENCES

Hybrid grids

[1] Kallinderis, Y. Hybrid Grids and their Applications. Chapter 35, *Handbook of Grid Generation*, Editors: Thompson, J.F., Soni, B.K. and Weatherill, N.P., CRC Press (1999).

Hybrid grid generation

[2] Kallinderis, Y., Khawaja, A., and McMorris, H. Hybrid Prismatic/Tetrahedral Grid Generation for Viscous Flows Around Complex Geometries. *AIAA J.* (1996) **34**:291-298.

[3] McMorris, H. and Kallinderis, Y. Octree-Advancing Front Method for Generation of Unstructured Surface and Volume Meshes. *AIAA J.* (1997) **35**:976-984.

[4] Khawaja, A. and Kallinderis, Y. Hybrid Grid Generation for Turbomachinery and Aerospace Applications. *Int. J. Num. Meth. Engng* (2000) **49**:145-166.

Element-type independent flow solvers

[5] Kallinderis, Y. and Nakajima, K. Finite-Element Method for Incompressible Viscous Flows with Adaptive Hybrid Grids. *AIAA J.* (1994) **32**:1617-1625.

[6] Schulz, K. and Kallinderis, Y. Unsteady Flow Structure Interaction for Incompressible Flows Using Deformable Hybrid Grids. *J. Comput. Phys.* (1998) **143**:569-597.

[7] Ahn, H. T. and Kallinderis, Y. Strongly coupled flow/structure interactions with a geometrically conservative ALE scheme on general hybrid meshes. *J. Comput. Phys*. (2006) **219**:671-696.

[8] Kallinderis, Y. A 3-D Finite-Volume Method for the Navier-Stokes Equations with Adaptive Hybrid Grids. *J. Appl. Num. Math*. (1996) **20**:387-406.

[9] Kallinderis, Y., Vitsas, P. and Menounou, P. A Low Order Flow/Acoustics Interaction Method for the Prediction of Sound Propagation using 3D Adaptive Hybrid Grids. *J. Comput. Phys*. (2012) **231**:6121-6138.

Parallel flow simulations with adaptive hybrid meshes

[10] Kallinderis, Y. and Vidwans, A. Generic parallel adaptive-grid Navier-Stokes algorithm. *AIAA J.* (1994) **32**:54-61.

[11] Minyard, T. and Kallinderis, Y. Octree Partitioning of Hybrid Grids for Parallel Adaptive Viscous Flow Simulations. *Int. J. Num. Meth. Fluids.* (1998) **26**:57-78.
[12] Kavouklis, C. and Kallinderis, Y. Parallel adaptation of general three-dimensional hybrid meshes. *J. Comput. Phys.* (2010) **229**:3454-3473

Grid adaptation

[13] Kallinderis, Y. and Baron, J. R. Adaptation Methods for a New Navier-Stokes Algorithm. *AIAA J.* (1989) **27**:37-43.
[14] Chen, A. and Kallinderis, Y. Adaptive Hybrid Grids for 3-D Incompressible Flows. *Int. J. Num. Meth. Fluids*. (1998) **26**:1085-1105.
[15] Kallinderis, Y. and Kavouklis, C. A Dynamic Adaptation Scheme for General Hybrid Meshes. *Comp. Meth. Appl. Mech. Engng.* (2005) **194**:5019-5050.
[16] Kallinderis, Y., Lymperopoulou, E.M., Spyridonos, G. and Antonellis, P. A study of properties of adaptive quadratic grids for three-dimensional near-surface field computations. *Int J Num. Meth Fluids*. (2019) **91**:63–96.

Error and grid interfaces

[17] Kallinderis, Y. Numerical treatment of grid interfaces for viscous flows, *J. Comput. Phys.* (1992) **98**:129-144.
[18] Fotia, S. and Kallinderis, Y. Quality index and improvement of the interfaces of general hybrid grids. *Proc. Engng* (2014) **82**:416-427.

Grid-based error estimation

[19] Kallinderis, Y. and Kontzialis, C. A priori mesh quality estimation via direct relation between truncation error and mesh distortion. *J. Comput. Phys.* (2009) **228**:881-902.
[20] Kallinderis, Y. and Fotia, S., A priori mesh quality metrics for three-dimensional hybrid grids, *J. Comput. Phys.* (2015) **280**:465-488.

Solution-based error estimation

[21] Kallinderis, Y., Lymperopoulou, E. M. and Antonellis, P. Flow feature detection for grid adaptation and flow visualization. *J. Comput. Phys.* (2017) **341**:182-207.
[22] Kallinderis, Y., Lazaris, P. and Antonellis, P. Detection of multiple interacting features of different strength in compressible flow fields. *J. Comput. Phys*. (2023) **477**:111948.